

Large-Eddy Simulations of Turbulent Flow for Grid-to-Rod Fretting in Nuclear Reactors

LA-UR 12-26572

J. Bakosi^a, M.A. Christon^a, R.B. Lowrie^a, L.A. Pritchett-Sheats^a, R.R. Nourgaliev^b

^a{jbakosi, christon, lowrie, lpritch}@lanl.gov

Corresponding author: J. Bakosi (jbakosi@lanl.gov, tel: +1-505-663-5607, fax: +1-505-663-5504)

Computational Physics Group (CCS-2)

Computer, Computational and Statistical Sciences Division

Los Alamos National Laboratory

Los Alamos, NM 87544

^brobert.nourgaliev@inl.gov

Reactor Safety Simulation Group

Thermal Science and Safety Analysis Department

Idaho National Laboratory

Idaho Falls, ID 83415

Abstract

The grid-to-rod fretting (GTRF) problem in pressurized water reactors is a flow-induced vibration problem that results in wear and failure of the fuel rods in nuclear assemblies. In order to understand the fluid dynamics of GTRF and to build an archival database of turbulence statistics for various configurations, implicit large-eddy simulations of time-dependent single-phase turbulent flow have been performed in 3×3 and 5×5 rod bundles with a single grid spacer. To assess the computational mesh and resolution requirements, a method for quantitative assessment of unstructured meshes with no-slip walls is described. The calculations have been carried out using Hydra-TH, a thermal-hydraulics code developed at Los Alamos for the Consortium for Advanced Simulation of Light water reactors, a United States Department of Energy Innovation Hub. Hydra-TH uses a second-order implicit incremental projection method to solve the single-phase incompressible Navier-Stokes equations. The simulations explicitly resolve the large scale motions of the turbulent flow field using first principles and rely on a monotonicity-preserving numerical technique to represent the unresolved scales. Each series of simulations for the 3×3 and 5×5 rod-bundle geometries is an analysis of the flow field statistics combined with a mesh-refinement study and validation with available experimental data. Our primary focus is the time history and statistics of the forces loading the fuel rods. These hydrodynamic forces are believed to be the key player resulting in rod vibration and GTRF wear, one of the leading causes for leaking nuclear fuel which costs power utilities millions of dollars in preventive measures. We demonstrate that implicit large-eddy simulation of rod-bundle flows is a viable way to calculate the excitation forces for the GTRF problem.

1. Introduction

Within the core of a pressurized-water nuclear reactor (PWR), water flow is used to cool the hot irradiated fuel rods. The grid-to-rod fretting (GTRF) problem in such reactors is a flow-induced vibration problem that results in wear and failure of the rods. GTRF wear is one of the leading causes for leaking nuclear fuel and costs power utilities millions of dollars in preventive measures. In order to understand the root causes of such fuel leaks, we inves-

tigate the complex turbulent coolant flow around fuel-rod bundles. Our ultimate goal is to accurately predict the turbulent excitation forces on the fuel rods, along with the coupled structural response of the rods and their supports. To date, it has not been possible to completely characterize the flow-induced fluid-structure interaction (FSI) problem for GTRF. Indeed, given the incompressible nature of the coolant, the relatively high Reynolds number, and the flexible character of the fuel rods and

spacers, the FSI problem at the reactor core scale is daunting.

As pointed out by Païdoussis [1], there are a number of flow-induced vibration problems in a nuclear power plant that involve the reactor, associated piping, heat exchangers, steam generators, and ancillary diagnostic equipment. Pettigrew, et al. [2] also consider a broad array of flow-induced vibration problems albeit specialized to the CANDU reactor configuration. A complete review of the work associated with all possible flow-induced reactor vibration problems is far beyond the scope of this work. However, a brief overview of some of the work related to the application of computational fluid dynamics (CFD) for fretting problems is presented here.

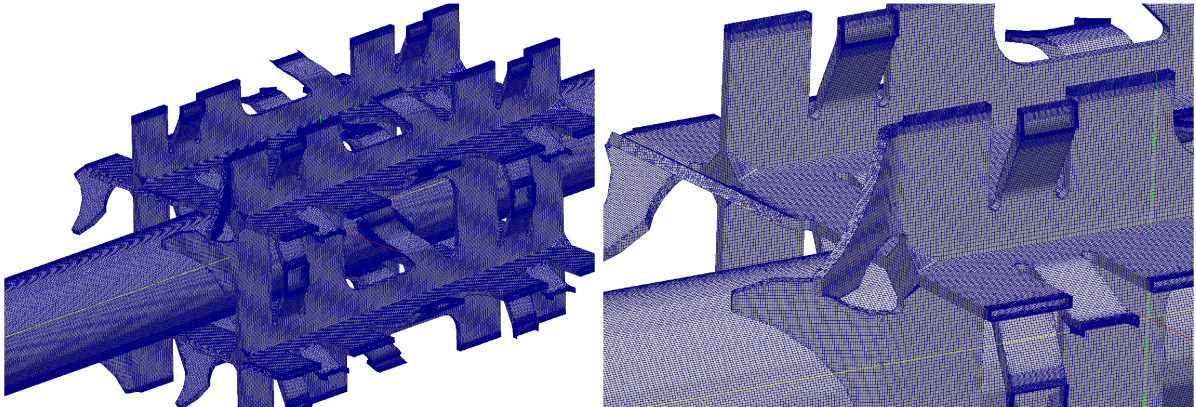
The work by Ikeno and Kajishima [3] relied on large-eddy simulation (LES) of the flow downstream of mixing vanes in a rod bundle. They used an immersed-boundary technique to treat the complex geometry and a dynamic subgrid-scale model to examine the mixing grid wake and downstream swirl. Benhamadouce, et al. [4] performed an LES of the flow in the subchannels surrounding a single rod, and subsequently used the turbulent forces to compute the elastic vibration of the fuel rod. Here, a relatively coarse mesh with 8 million cells was used for the $Re = 30,000$ flow. Related work by Kim [5, 6, 7] has considered grid-to-rod fretting wear models for PWRs as well as the effects of the rod support conditions on fuel rod vibration.

Conner, et al. [8] present a validation study using a 5×5 rod bundle, representative of a fuel assembly and compare the mixing-vane-induced swirl with particle image velocimetry (PIV) data. Here, the RNG $k-\epsilon$ model was used with $40 \leq y^+ \leq 100$ to compute a steady-state solution. Yan, et al. [9] performed time-accurate CFD computations and compared the effect of the so-called “protective grid” at the fuel-inlet region of a reactor. For this study, meshes with 7, 16 and 60 million cells were used. Here, it was shown that a time-accurate CFD calculation can be used to determine transient fuel rod forces for subsequent dynamic analyses. This work also demonstrated that the protective grid significantly reduces flow-induced vibration at the reactor core inlet. Zhang and Yu [10], and Bhattacharya, et al. [11] have performed large-eddy simulations using the CANDU fuel bundles and the vortex shedding phenomena associated with the endplates. The work by Delafontaine and Ricciardi [12] used LES to determine the time-dependent rod forces down-

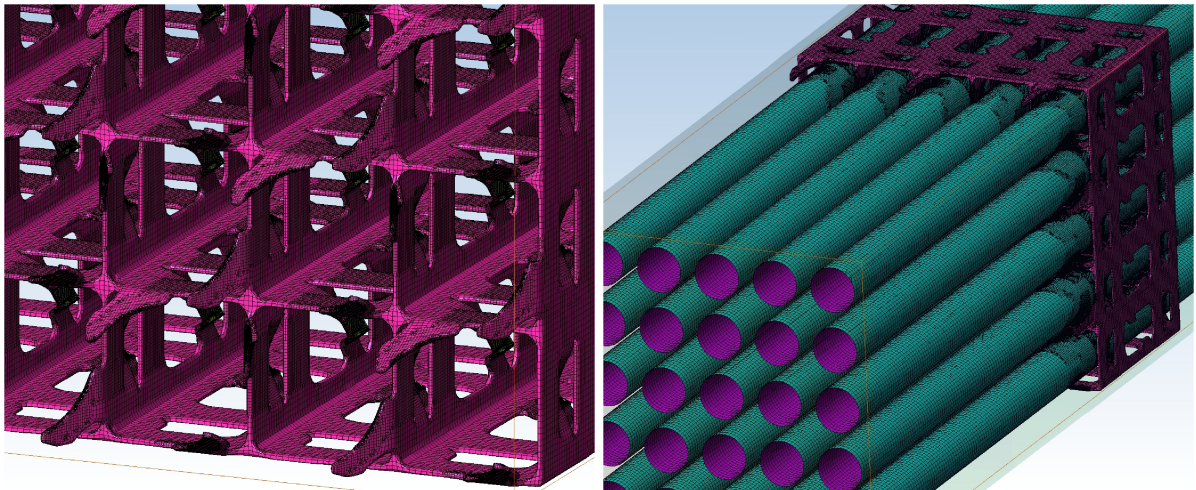
stream of a 3×3 rod bundle. Here detailed information about the angular variation of pressure forces on the fuel rod are presented. The work by Liu, et al. [13] considered fluid-structure interaction in simplified fuel assemblies where a rod buckling instability was demonstrated to occur with large axial flow velocities. Related work was performed by Mohany and Hassan [14] to represent the flow-induced vibration and associated fretting wear in a CANDU fuel bundle.

Our investigation of LES for GTRF centers on CFD simulations using Hydra-TH, a thermal-hydraulics code developed at Los Alamos National Laboratory. Hydra-TH can compute high-Reynolds number turbulent flows over arbitrarily complex geometries. There are tens of thousands of fuel rods in a PWR, and computing the flow over all of them simultaneously, with the fidelity required for GTRF, is not feasible on today’s computers. Instead, this study concentrates on representative 3×3 and 5×5 rod-bundle configurations, for which sample computational meshes are shown in Figure 1. The 3×3 and 5×5 geometries were extracted from a 17×17 fuel assembly found in a typical PWR. There is a large degree of symmetry in the fuel assembly which makes this geometrical simplification a reasonable approximation. The coolant flow generally moves axially on the outside of the fuel rods. A “grid spacer” (rod support structure) is also shown, which contains mixing vanes that stir the flow in order to enhance heat transfer from the rod to the coolant flow. This stirring, along with the high Reynolds number of the flow, results in a complex turbulent flow that is believed to be the primary driver of GTRF-induced failure downstream of the grid spacer and mixing vanes.

The current engineering practice for the GTRF problem is to compute turbulent flow solving the Reynolds-averaged Navier-Stokes (RANS) equations augmented by a turbulence model. RANS models, used in either steady (RANS) or unsteady (URANS) mode, directly compute the flow statistics by solving for only the mean field values, and depending on the model, the second moments. For example, the $k-\epsilon$ model, see e.g. [15], is a popular way to approximate the *effects of fluctuations on the mean velocity*. However, it is important to appreciate that the main goal of the $k-\epsilon$ model is to provide closure for the mean velocity via the time scale $\sim k/\epsilon$. Consequently, one can expect a statistically meaningful description of the mean but less of the fluctuations, e.g., k or ϵ , themselves, as only



(a) Surface mesh for the center rod and spacer in the 47M-cell 3×3 rod bundle.



(b) Surface mesh of the spacer with mixing vanes (left) and of the rods and spacer (right) in the 14M-cell 5×5 rod bundle.

Figure 1: Surface meshes of the 5×5 and 3×3 rod bundle geometries.

their effect on the mean is represented. If the second moments, e.g. the fluctuations about the mean, are also important, a model with a higher level of description is required. For example, second-order RANS models directly compute not only the means but the root-mean-square (RMS) fields as well.

RANS models, including the $k-\epsilon$ model, widely adopt the Boussinesq (or turbulent viscosity) hypothesis whose limitations and their failure to adequately predict even simple turbulent flows are well-known [15]. Therefore, it is best practice to compute a problem by a method that provides a higher level of description before a RANS model can be operationally used with confidence. One such technique is LES, which provides a direct representation of the energy-containing motions of a turbulent flow. Compared to RANS, LES has the advan-

tage of describing unsteady, large-scale turbulent structures, and hence can be used to study phenomena such as the unsteady loads of the GTRF problem. In LES, the dynamically small scales are modeled, while the large unsteady motions are computed without approximation. If the small scales are universal, i.e. Kolmogorov's hypothesis holds, as in many engineering applications, LES is known to provide excellent results, as the effect of the small (modeled) scales on the large scales are negligible.

We believe a problem such as GTRF must be studied with LES before operational use of unsteady RANS can be attempted. Consistent with this idea, this study is a step towards (1) understanding the fluid dynamics of GTRF, (2) assessing the computational resolution requirements, and (3) building a database of turbulence statistics for

different configurations based on which rational decisions for future computations can be made and the development of a GTRF-specific RANS model can be attempted.

The rest of this paper is organized as follows. Hydra-TH is briefly reviewed in §2, then §3 discusses mesh generation and presents a method for quantitative mesh assessment for complex geometries. The flow computations are discussed in §4. Finally, §5 gives a summary, while §6 points to future directions.

2. Overview of Hydra-TH

Hydra-TH is a thermal hydraulics code developed at Los Alamos National Laboratory for the Consortium for Advanced Simulation of Light water reactors (CASL).¹ The code is being developed to address a number of single and multiphase problems ranging from GTRF to departure from nucleate boiling.

Hydra-TH is a massively parallel code built on the Hydra Toolkit. The Hydra Toolkit is written in C++ and provides a rich suite of lightweight high performance components that permit rapid application development, supports multiple discretization techniques, provides I/O interfaces to permit reading and writing multiple file formats for meshes, plot data, time-history, surface and restart output. The Toolkit also provides run-time parallel domain decomposition with data-migration for both static and dynamic load-balancing. Linear algebra is handled through an abstract virtual interface that enables the use of both native and external libraries such as PETSc² and Trilinos³.

Hydra-TH also contains a rich suite of turbulence models that range from LES to detached-eddy and various RANS models. The code relies on a hybrid finite-volume/finite-element discretization for incompressible flow that provides a stable and accurate discretization while preserving local conservation properties important in many thermal hydraulics applications. Hydra-TH also supports the use of hybrid meshes that permit the resolution of boundary layers on very complex geometries.

For the incompressible Navier-Stokes formulation, all transport variables are cell-centered

and treated with a locally conservative discretization that includes a high-resolution monotonicity-preserving advection algorithm. The spatial discretization is formally derived using a discontinuous-Galerkin framework that, in the limit, reduces to a locally-conservative finite-volume method with reconstruction and second-order spatial accuracy. The advection algorithm is designed to permit both implicit and explicit advection with the explicit advection targeted primarily at volume-tracking with interface reconstruction. The available time-integration methods include backward-Euler and the neutrally-dissipative trapezoidal method. The implicit advective treatment delivers unconditional stability for scalar transport equations and conditional stability for the momentum equation. As opposed to the transport variables, which are cell-centered, the pressure is node-centered. A Poisson-equation is solved for a Lagrange multiplier from which the pressure is computed. The divergence-free constraint on the velocity field is enforced via a projection algorithm, similar to [16, 17]. The code has been run on up to ten thousand compute cores using 100-million-cell meshes, and is being developed to exploit the multiple levels of hybrid parallelism of future compute architectures. More details on the Hydra Toolkit and its incompressible solver are given in the Hydra-TH Theory manual [18].

3. Mesh Generation and Quality Assessment

This section discusses the computational meshes and associated quality metrics for GTRF LES computations. §3.1 presents two different meshing technologies used in this work. §3.2 presents a method for quantitative assessment of unstructured meshes with no-slip walls. In §3.3 an evaluation of the two series of meshes is given.

3.1. Mesh generation for GTRF

In one of our earlier studies [19], several desirable characteristics of the computational meshes for LES were discussed, and include the following.

1. Sufficient overall mesh resolution for capturing the important energy-containing features of the flow.
2. Smooth transitions in regions downstream of the spacer to avoid unphysical aliasing (i.e., numerical back-scatter) of the kinetic energy from smaller to larger scales.

¹www.casl.gov

²www.mcs.anl.gov/petsc

³trilinos.sandia.gov

3. High quality boundary layers to adequately but economically resolve the complex turbulent flow in the vicinity of walls.

In calculations with heat transfer, point 3 above may be particularly important due to (1) the highly inhomogeneous and anisotropic nature of the flow near walls, and (2) the potentially first-order influence of the mesh quality on the simulation.

As an alternative to the Cubit mesh generator,⁴ used to generate the meshes for the calculations in [19], we explored Numeca’s Hexpress/Hybrid, a.k.a. Spider,⁵ meshing tool. Spider’s shrink-wrap meshing technology is quite different from that of Cubit and allows for fully automatic generation of body fitted meshes on arbitrarily complex geometries. Spider meshes are unstructured, hex-dominant, and conformal, containing hexahedra, tetrahedra, wedges, and pyramids. As a consequence, extremely complex geometries can be discretized with good quality elements. Furthermore, Spider is capable of generating high-quality viscous layers; its configuration is based on a simple text file, though a graphical interface is also available; and it is easy to use in batch mode, yielding fast throughput for generating a series of meshes for convergence studies and uncertainty quantification.

We have generated a series of Spider meshes for the rod-bundle geometry developed at Westinghouse Electric Company for both 3×3 and 5×5 rod configurations. The dimensions of the geometry, used for mesh generation and computations, are the same as in [20]. The approximate cell-count for the 3×3 meshes are 2 million (M), 7M, 14M, 27M, 30M, 47M, 80M, and 185M, and for the 5×5 meshes are 14M and 96M. Example snapshots of the surface mesh for the rod and spacer geometries in the 3×3 and 5×5 rod-bundle geometries are displayed in Figure 1. Visual inspection reveals uniform cell sizes inside of the domain with targeted refinement in corners and edges in the vicinity of the spacer and symmetry planes (not shown). Compared to the Cubit meshes, discussed in [19], which had abrupt $\sim 4\Delta x$ jumps downstream of the spacer, the Spider meshes have no visible abrupt transitions in cell sizes and there are smooth transitions from refined corners inside the domain. These features are desirable from the viewpoint of obtaining quality LES results. The meshes, resulting in different number of total cells, have been generated by

changing the single parameter, BASEH, in the Spider input deck. BASEH defines the minimum resolution, characteristic of the largest cell size. This yields different-resolution and similar meshes. The meshes discussed in this study contain no targeted boundary layer refinement close to walls. Generating meshes with power-law-graded boundary layers using Spider is a subject of future work.

In summary, we are satisfied with Spider as a tool for mesh generation: it is relatively easy to use, fast, and automatically generates high-quality meshes for extremely complex geometries, required for the GTRF problem. As an example, the 96M 5×5 mesh is generated in only 80 minutes on an 8-core workstation with 48GM RAM. Spider is a shared-memory parallel code and its approximate memory requirement is 0.5GB RAM per million cells generated; it can export the mesh in the latest Exodus-II file format with an HDF5 container, required for mesh sizes beyond ~ 60 M hex cells.

3.2. Mesh quality assessment

In CFD simulations of wall-bounded turbulent flows, the mesh quality along no-slip walls has a first-order influence on the accuracy of the numerical solution. Boundary elements need to be small and uniform in the wall-normal direction for adequately resolved boundary layers. However, for very complex flow geometries the size and uniformity of the cells along walls are difficult to maintain during mesh generation. Clearly, there is a need for a quantitative assessment of the quality of complex meshes preferably *a priori* of large-scale LES simulations.

In CFD engineering practice, the quantity y^+ is commonly used to assess the mesh at no-slip walls. The distance from the wall, measured in viscous lengths, or wall-units, is defined by

$$y^+ \equiv \frac{y}{\nu} \sqrt{\frac{\tau_w}{\rho}}, \quad (1)$$

where y , ν , τ_w , and ρ denote the (dimensional) distance from the wall (in the wall-normal direction), kinematic viscosity, wall-shear stress, and fluid density, respectively. As y^+ is similar to a local Reynolds-number, its magnitude can be expected to determine the relative importance of viscous and turbulent processes. Values of $y^+ \approx 1$ are recommended for LES with full wall-resolution, and $y^+ \gtrsim 20$ for RANS models with wall-functions. The value of y^+ can be computed in each computational

⁴<http://cubit.sandia.gov>

⁵<http://www.numeca.be/index.php?id=hexhyb>

cell along no-slip walls for a given Reynolds number and mesh, in general, yielding a different value in each cell. For unstructured meshes, the y^+ field is generally non-uniform along a surface.

To assess a mesh *a priori* of computation, a physically realistic y^+ field, defined by Eq. 1, must be obtained with minimal computational effort. In a numerical solution of the Navier-Stokes equations, the y^+ field obtained after the first time step can be used to assess the mesh if (and only if) the initial and boundary conditions are consistent with the dynamical level of approximation of the computed flow. In constant-density single-phase flows, this consistency amounts to a divergence-free velocity field and a consistent pressure, both satisfying the prescribed initial and boundary conditions.

The incompressible flow solver in Hydra-TH is based on a second-order implicit projection algorithm that uses a pressure-Poisson equation to continuously project the velocity field to a divergence-free velocity space at each time-step. Given a set of user-prescribed initial and boundary conditions, the initial startup procedure (before $t=0$) computes the solution of a Poisson equation for a Lagrange multiplier. Then a subsequent projection of the prescribed velocity field to a divergence-free subspace ensures that (1) the velocity field is divergence-free, (2) the velocity is consistent with the pressure, and (3) both fields satisfy the prescribed initial and boundary conditions for an incompressible flow. This procedure guarantees that basic solvability conditions [18] are satisfied at $t=0$ and that a mathematically and numerically well-posed Navier-Stokes problem is integrated for $t>0$. For details on the startup procedure in Hydra-TH, see [18].

The y^+ fields, discussed below, have been obtained after the above startup procedure, solving the constant-density Navier-Stokes equations, for a single time step, and serve as the basis of the mesh quality assessment *a priori* of computations. We emphasize that the y^+ field computed after the first time step is approximate: it depends on the mesh, the Reynolds number, and the turbulence model employed to compute τ_w , and is only constant when the flow is statistically stationary. Ideally, a more accurate y^+ could be obtained after the flow has reached a statistically stationary state. However, for large meshes, obtaining a statistically stationary state may require thousands of time steps and thus it is not economical as a quick *a priori* mesh assessment. Instead, we rely on the approximate but physically and mathematically consistent y^+ field

after the first time step. As y^+ depends on the turbulence model, its values (in an absolute sense) are of limited value: the main goal of the *a priori* mesh assessment is the evaluation of the mesh quality with respect to the mesh generators and the generated meshes.

3.3. Evaluation of the mesh quality

Figure 2 shows the spatial y^+ distribution for the same Reynolds number and geometry for two different meshes, generated by different mesh generation technologies. The mesh in Figure 2(a) is generated by Spider, while the mesh in Figure 2(b) is produced by Cubit.

While the smallest and largest y^+ values on these two meshes are comparable, the fields are very different. The y^+ on the Spider mesh appears to be much smoother and low y^+ values indicate highly refined edges and corners. Compared to the Spider mesh, the Cubit mesh exhibits a much more checkerboard-like pattern, indicating a larger spatial variation of y^+ on the surface. A uniform y^+ distribution is desirable for a predictable simulation quality. For example, sudden changes in y^+ (e.g., due to abrupt changes in the cell sizes along walls) may perturb an otherwise smooth boundary layer, resulting in artificial adverse pressure gradients and unphysical boundary-layer separation. This is particularly important in wall-resolving LES, as the simulations must adequately represent the highly inhomogeneous and anisotropic nature of the turbulent flow in the vicinity of walls. In RANS simulations, more uniform y^+ fields are reassuring in that the assumptions, such as zero mean pressure gradient, used in the development of wall-functions, are satisfied.

Quantitative *a priori* metrics that could be used to assess non-uniform y^+ fields on a complex surface, such as around the spacer and mixing vanes, depicted in Figure 2, may be defined based on the statistical distributions of the y^+ field. Such a distribution may be generated by counting up the y^+ values of the cells adjacent to a surface and grouping them into equally-sized bins between their extremes. Instead of counting each y^+ value as 1, we generate an area-weighted y^+ histogram by counting values of the wall-attached cell area times the y^+ along the surface. Such an area-weighted histogram is displayed in Figure 3, corresponding to the y^+ distributions of the two meshes in Figure 2.

The mean of the histograms in Figure 3 may be used as a quantitative metric to assess the *average*

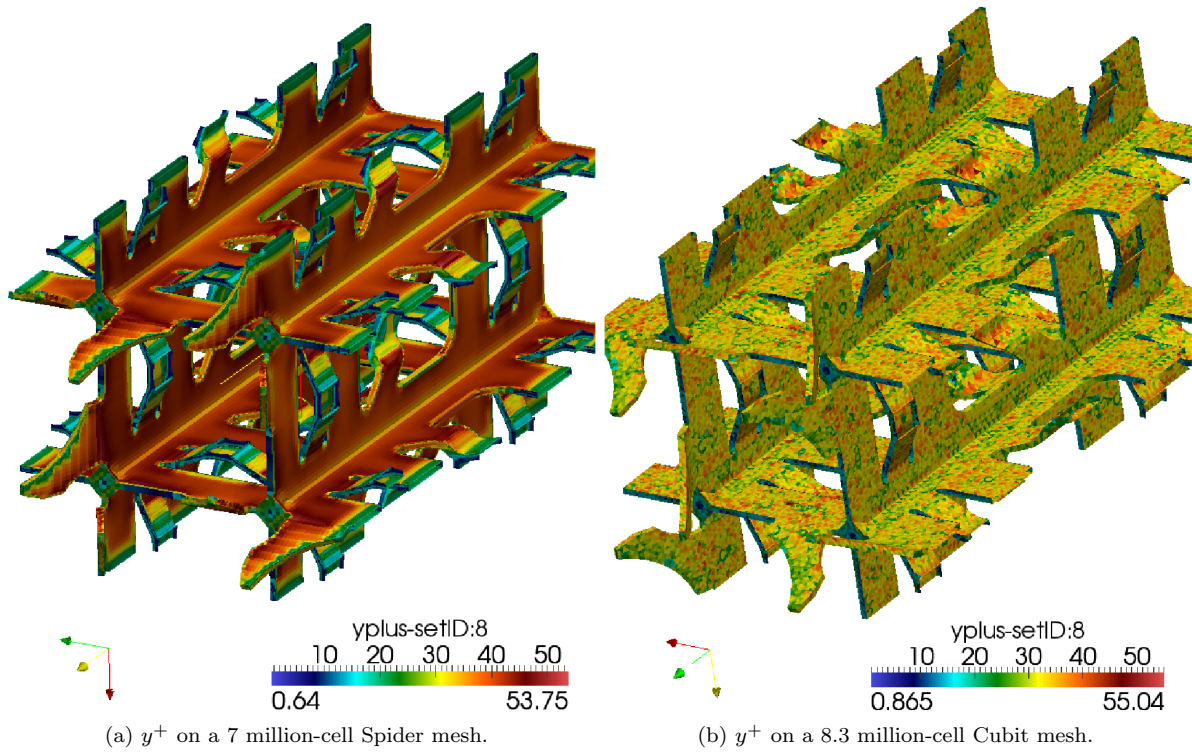


Figure 2: Spatial distribution of y^+ for two different meshes for the same geometry and Reynolds number.

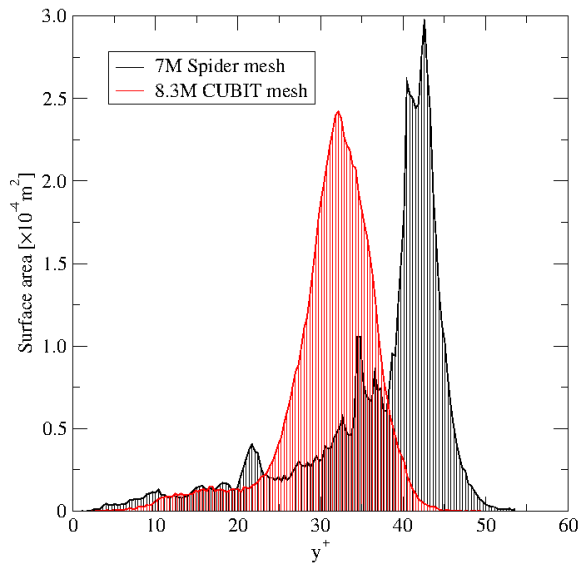


Figure 3: Cell-area-weighted histograms of y^+ for the 7M Spider and 8.3M Cubit meshes for the same geometry and Reynolds number. The histograms correspond to the meshes and spatial y^+ distributions in Figure 2.

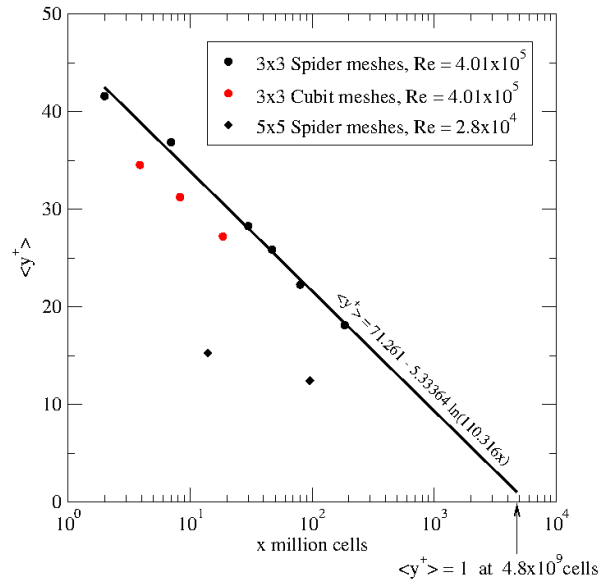


Figure 4: $\langle y^+ \rangle$ vs. number of cells for all meshes generated for the 3×3 and 5×5 configurations.

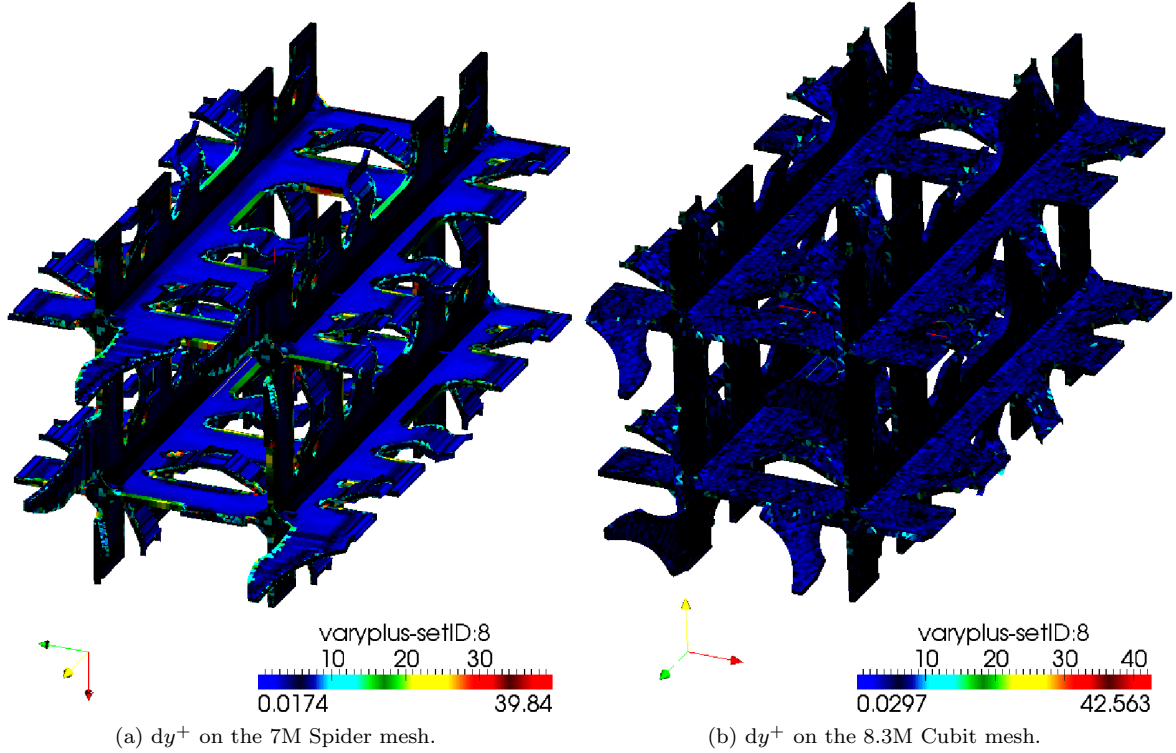
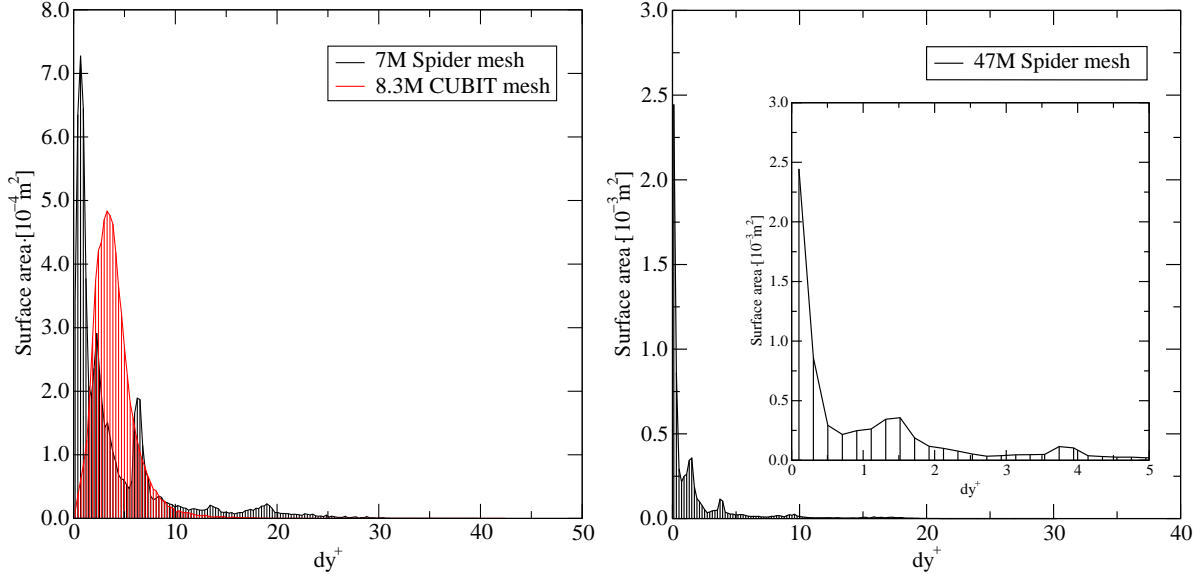


Figure 5: Spatial distribution of the variation of y^+ , dy^+ , for Spider and Cubit meshes for the same geometry and Reynolds number.

Rod bundle	Mesh	Generator	No. of elements	y_{min}^+	y_{max}^+	$\langle y^+ \rangle$	$TV(y^+)/A$
3×3	2M	Spider	2.6M	1.55	73.41	41.58	0.38
	7M		7.8M	0.82	53.57	36.85	0.27
	30M		30.0M	0.72	43.18	28.26	0.21
	47M		46.8M	0.70	40.92	25.85	0.20
	80M		83.2M	0.34	34.25	22.25	0.15
	185M		185.4M	0.35	29.87	18.10	0.16
5×5	14M	Spider	14.2M	0.29	22.04	15.24	0.11
	96M		96.3M	0.31	16.42	12.41	0.09
3×3	3.9M	Cubit	3.9M	1.87	61.38	34.52	0.40
	8.3M		8.3M	1.99	53.70	31.23	0.35
	18.6M		18.7M	0.85	45.41	27.20	0.30

Table 1: Statistics of computational meshes generated for the GTRF problem on 3×3 and 5×5 rod-bundle geometries. The Spider meshes are all hex-dominated hybrid meshes, containing hexahedra, pyramids, tetrahedra, and wedges; the Cubit meshes contain pure hexahedra. The y^+ fields are computed along the spacer surfaces, the most complex part of the geometry where no-slip/no-penetration boundary conditions are imposed. The Reynolds number for the 3×3 rod-bundle is $Re_{D_h} = 4.01 \times 10^5$, corresponding to [19] and [20]. The Reynolds number for the 5×5 geometry is $Re_{D_h} = 28.0 \times 10^3$, corresponding to [21]. The extremes of the y^+ fields, y_{min}^+ and y_{max}^+ , denote the extents of the y^+ histograms, while $\langle y^+ \rangle$ and the (total variation) $TV(y^+)$ are the mean of the y^+ histograms and the integral of the dy^+ histograms, respectively. The total variation is normalized by the total surface of the spacer, A .



(a) dy^+ histograms for the 7M Spider and 8.3M Cubit meshes, corresponding to the meshes and spatial dy^+ distributions in Figure 5.

(b) dy^+ histogram for the 47M Spider mesh.

Figure 6: Cell-area-weighted histograms of the variation of y^+ , for the spacer meshes for the same geometry and Reynolds number. The closer the histogram to a delta-peak at $dy^+ = 0$, the more uniform the y^+ field is distributed along the surface.

y^+ on a complex surface with no-slip boundary conditions. The mean can be computed by numerically estimating the integral

$$\langle y^+ \rangle \equiv \frac{\int y^+ f(y^+) dy^+}{\int f(y^+) dy^+} \approx \frac{\sum y^+ f(y^+) \Delta y^+}{\sum f(y^+) \Delta y^+}, \quad (2)$$

where $f(y^+)$ denotes the function values of the area-weighted histogram, such as in Figure 3. The mean y^+ , $\langle y^+ \rangle$, computed for all the meshes generated is shown in Table 1 and displayed in Figure 4.

The spatial uniformity of the y^+ field is also of interest. To define a useful metric that characterizes the uniformity, the spatial variation of y^+ is extracted based on the y^+ field. The variation of y^+ is computed by visiting each surface cell and finding the maximum difference among the y^+ of the given cell and that of its immediate neighbors. This yields a new scalar field, which we call dy^+ , whose area-weighted histogram is computed using the same method as that of y^+ , discussed previously. The spatial distribution of the y^+ variation fields for the 7M Spider and 8.3M Cubit meshes are shown in Figure 5. This confirms the earlier observation that the Spider mesh is smoother, while

the y^+ varies more significantly in the Cubit mesh. This is quantified in the histograms shown in Figure 6. Compared to the y^+ histograms, the dy^+ histograms are only defined for $dy^+ \geq 0$. The theoretical ideal dy^+ histogram is a Dirac delta function at $dy^+ = 0$. Larger dy^+ values correspond to a larger surface area covered by given y^+ variation. While the dy^+ histogram for the Spider mesh has a large peak close to 0, the peak for the Cubit mesh is displaced to the right, indicating that there is significant variation in y^+ for most of the surface area. The differences in the uniformity of y^+ can be explained by the differences in the mesh generation strategies. The Spider meshes are generated by first inserting an initial layer of similar-size cells closely following the complex boundary and using different cell-types without truncating cells or geometry. In Cubit, the mesh is first generated using tetrahedra which then are dissected to yield an all-hex mesh, resulting in non-uniform cell sizes along walls. Figure 6 shows the dy^+ histogram for a finer, 47M-cell, Spider mesh: the variations in y^+ is significantly reduced compared to the coarser 7M mesh. To quantify the uniformity with a single

scalar, one can estimate the total variation of y^+ by computing the total surface area under the dy^+ histograms:

$$\text{TV}(y^+) \equiv \int g(dy^+)d(dy^+) \approx \sum g(\Delta y^+)\Delta(\Delta y^+), \quad (3)$$

where $g(dy^+)$ denotes the function values of the area-weighted dy^+ histogram, such as in Figure 6. The total variation (TV) has also been computed for all meshes generated and displayed in Table 1 for comparison. The following observations can be made based on the data in Table 1:

- The mean y^+ monotonically decreases with increasing cell count, signaling an overall uniform increase of refinement with larger meshes; a prerequisite for meaningful mesh convergence studies and uncertainty quantification.
- The total variation of y^+ also monotonically decreases with increasing cell-count, i.e., relatively larger surface area is covered by more uniform-size wall-cells, an assurance of increasing mesh quality at walls, which minimizes unphysical perturbations in the wall-treatment, important for both LES and RANS simulations with wall-functions.
- Based on the dy^+ histograms and the total variation of y^+ , the quality of Spider meshes are clearly superior to those produced using Cubit.

Figure 4 shows a graphical representation of the $\langle y^+ \rangle$ column in Table 1. The $\langle y^+ \rangle$ is plotted for both series of Spider meshes for the 3×3 and 5×5 geometries, as well as for the series of Cubit meshes. While the Reynolds number is the same for the Cubit and Spider series of meshes for the 3×3 geometry, the $\langle y^+ \rangle$ for the 5×5 meshes are computed for a lower Reynolds number. This is the main reason for a significantly lower $\langle y^+ \rangle$ for the 5×5 meshes for similar total cell counts when compared to the 3×3 meshes. Both the Spider and the Cubit meshes exhibit a monotonic decrease in the mean y^+ with increasing cell count. The trends are all logarithmic. This is expected as none of these meshes have power-law-graded boundary-layer refinement at walls. The logarithmic fit extrapolates the trend for the 3×3 Spider meshes and predicts that to achieve $\langle y^+ \rangle \sim 1$ with this meshing strategy would require approximately 5 billion cells. This is clearly not practical, therefore the next step in

mesh generation for wall-resolving LES is to add power-law-graded boundary layer refinement.

In summary, a method for quantitative assessment of unstructured meshes with no-slip walls has been described. The two metrics, $\langle y^+ \rangle$ and $\text{TV}(y^+)$, have been used to assess mesh quality generated by two mesh generators for two rod-bundle geometries.

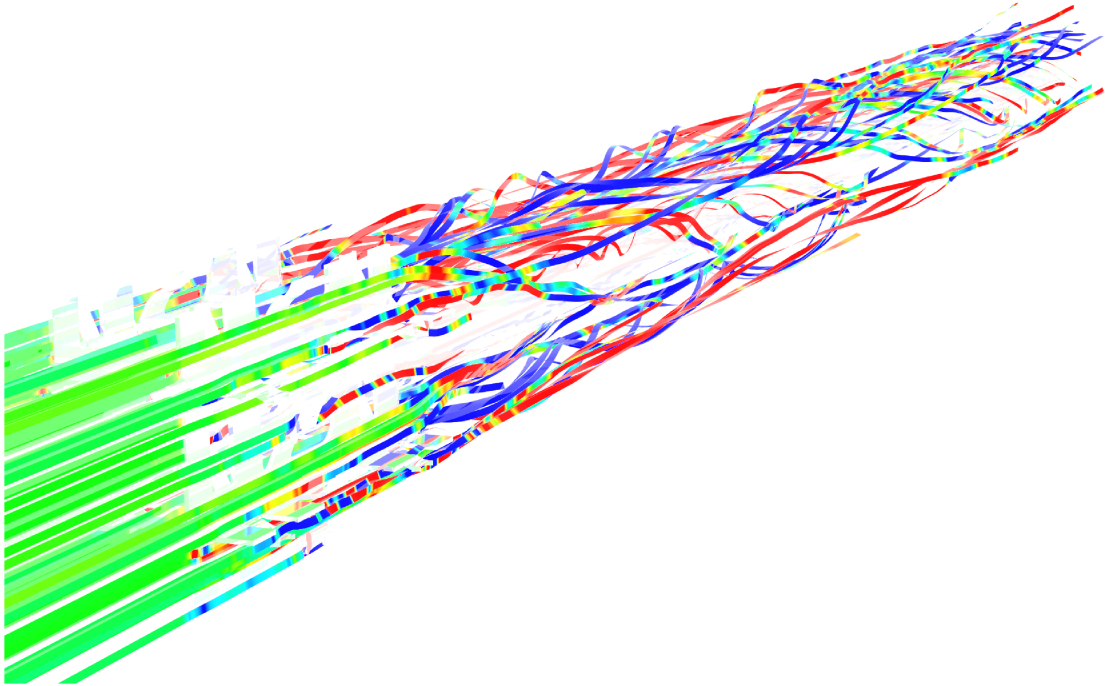
4. LES Calculations and Analysis

This section discusses the LES simulations using the Spider meshes for the 3×3 (§4.1) and 5×5 (§4.2) rod-bundle geometries, respectively. Our earlier study, [19], provides details on calculations using LES, detached-eddy, and the Spalart-Allmaras (URANS) turbulence models using the Cubit meshes, where it was determined that the most accurate GTRF forces are obtained with LES.

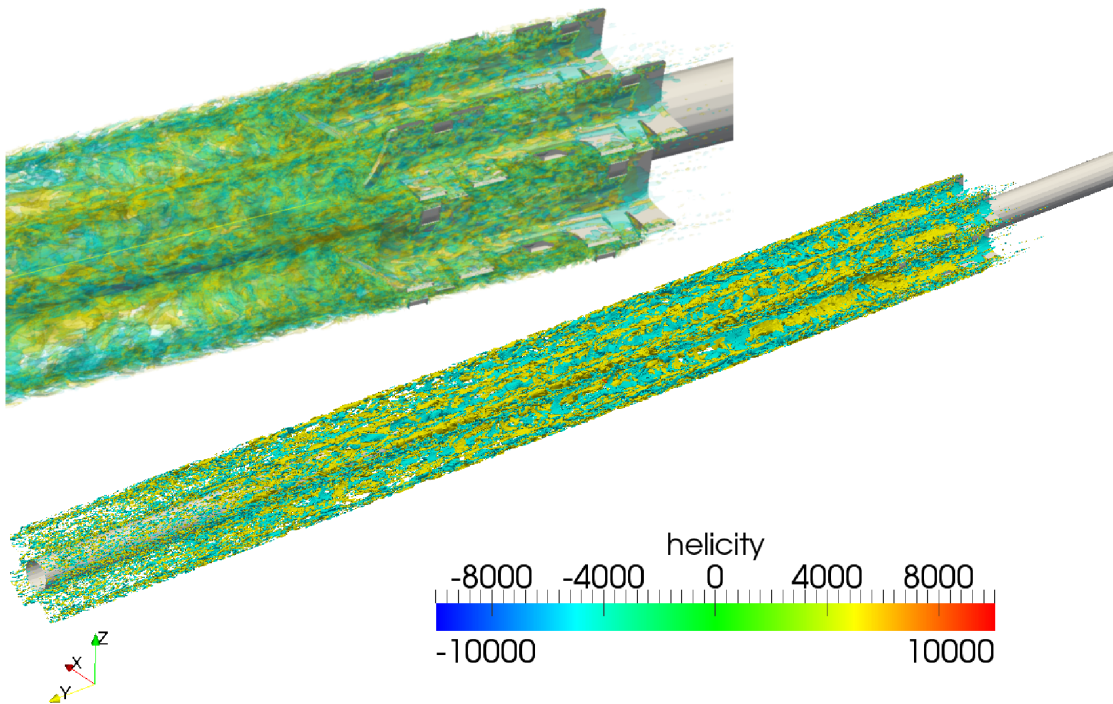
The flow geometry and the computational setup closely resembles that of Elmahdi, et al. [20], in which LES is documented using Star-CCM+ with the wall-adapted large-eddy unresolved-scale model of [22]. In [20] a central difference scheme, available in Star-CCM+, has been used with a “wall-blending factor”. In comparison, the Hydra-TH calculations, discussed below, do not use any particular treatment at no-slip, no-penetration boundaries. While Elmahdi, et al. use a maximum CFL of 1.0, the Hydra-TH simulations employ $CFL = 4.0$.

4.1. LES on the 3×3 Spider meshes

For the 3×3 calculations, the working fluid is water at a temperature of 394.2 K, a density of 942.0 kg/m^3 , and a dynamic viscosity of $2.32 \times 10^{-4} \text{ kg/m}\cdot\text{s}$. The inlet velocity is prescribed as $\mathbf{v} = (0, 0, 5) \text{ m/s}$. This corresponds to a Reynolds number, based on the rod diameter, of $Re_D = 1.93 \times 10^5$, while the Reynolds number based on the hydraulic diameter is $Re_{D_h} = 4.01 \times 10^5$. The hydraulic diameter is defined as $D_h = 4A_{flow}/P_{wet}$. The inlet velocity is constant. While this is certainly not a good approximation for modeling several grid-spans, a main goal of the current calculations is to facilitate a direct comparison to the data of Elmahdi, et al. [20], which prescribes the same inlet conditions. No-slip, no-penetration conditions are prescribed at the rod and spacer surfaces. At the outlet, the hydrostatic pressure is specified to be $p_h = 0.0$ in conjunction with a zero shear stress condition. No-penetration conditions



(a) Instantaneous velocity streamlines colored by helicity for the 2M Spider mesh.



(b) Instantaneous helicity isosurfaces for the 47M Spider mesh.

Figure 7: Instantaneous snapshots of velocity (\mathbf{v}) and helicity ($\mathbf{v} \cdot \boldsymbol{\omega}$) isosurfaces from using the 2M and 47M Spider meshes.

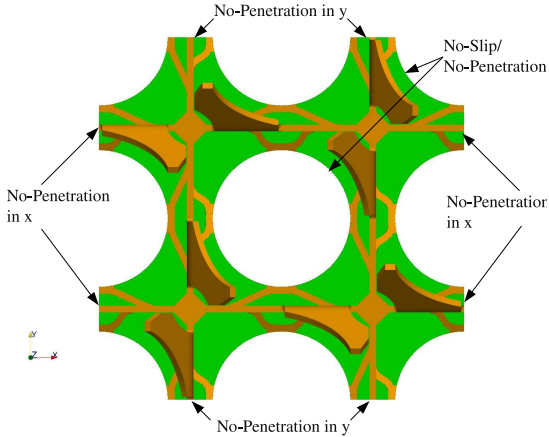


Figure 8: Boundary conditions on rod and spacer surfaces, and subchannel boundaries.

with in-plane slip were applied at the subchannel boundaries as shown in Figure 8. As only one grid-span of a 3×3 rod-bundle of the full reactor core is modeled, no attempt is made here to prescribe realistic PWR operating conditions. Our goal is to reproduce the simulation conditions in [20].

A qualitative picture of the instantaneous flow behind the mixing vanes is obtained by depicting the velocity streamlines with ribbons and isosurfaces of the instantaneous helicity field in Figure 7. The stream ribbons are for the coarsest 2M simulations, while the isosurfaces are for the 47M case. The vortices generated by the spacer and the mixing vanes are advected downstream. Figure 7(b) shows that the neutrally dissipative advection algorithm in Hydra-TH does an excellent job in maintaining the complex vortex structures far downstream.

Similar to our earlier LES calculations on the 3×3 rod-bundle [19], a series of preliminary coarse-mesh simulations were conducted using the Spider meshes to determine when a statistically stationary flow is achieved. The time-evolution of the domain-integrated kinetic energy (not shown) was used as an indicator. Based on the kinetic energy the time of approximately 0.1s, which corresponds to approximately 1.25 flow transits by which the domain-integrated kinetic energy has reached a statistically stationary state, was chosen as the starting point for collecting time-averaged flow statistics until the end of the simulation at $t = 1.0$ s.

LES calculations, using the 2M, 7M, 30M, 47M Spider meshes, discussed earlier, and additional ones with 14M and 27M meshes, have been carried out. The instantaneous pressure is plotted in Figure 9 for five different meshes. The pressure line plots have been extracted using a line along the rod, offset from the surface by $6.3698 \times 10^{-6} D$ where D is the rod diameter, and extending for the full length of the rod. The vertical lines in Figure 9 delineate the bounds of the spacer and the mixing vanes. It is reassuring that the pressure lines are qualitatively very similar for all mesh resolutions. Since the hydrostatic pressure at the outflow is fixed at $p = 0$, the value of the calculated inlet pressure determines the pressure drop over the whole domain. The pressure drop for the 47M Spider mesh is 11.425 kPa, however, this value does not seem to have converged for this series of calculations. In contrast to the pressure observed with the Cubit meshes [19], the pressure drop is monotonically increasing with mesh resolution – largely a consequence of the better boundary layer resolution compared to the Cubit meshes.

The mean pressure along the rod is also plotted in Figure 9 and indicates that the bulk of the of the pressure loss is due to the spacer. In spite of the turbulent flow induced by the spacer, the characteristic peaks and troughs in the profile of the mean pressure is very much reproducible throughout the spacer using the 2M, 7M, and 14M meshes. Downstream of the mixing vanes a slight wave in the mean pressure is apparent in the coarsest 2M-mesh simulation. The mean pressure using the 7M mesh appears as what one would intuitively expect for a turbulent pipe flow: from approximately $y = 0.175m$, the mean pressure decreases linearly.

The RMS pressure along the rod is plotted in Figure 10(a) for three Spider meshes. The fluctuating pressure force is probably the most important quantity to compute accurately for a reasonable representation of the forces acting on the fuel rods. The RMS pressure indicates the deviation in the pressure relative to the mean, and is correlated in an incompressible flow to local eddying motion. The figure shows that the RMS pressure peaks at the downstream end of the spacer for the 7M and 14M meshes. This is expected, since this is where the flow is separated with complex eddy structures, and where the level of turbulent kinetic energy is the largest. While the downstream locations of the peaks are somewhat aligned for the varying meshes, their amplitudes and downstream evolu-

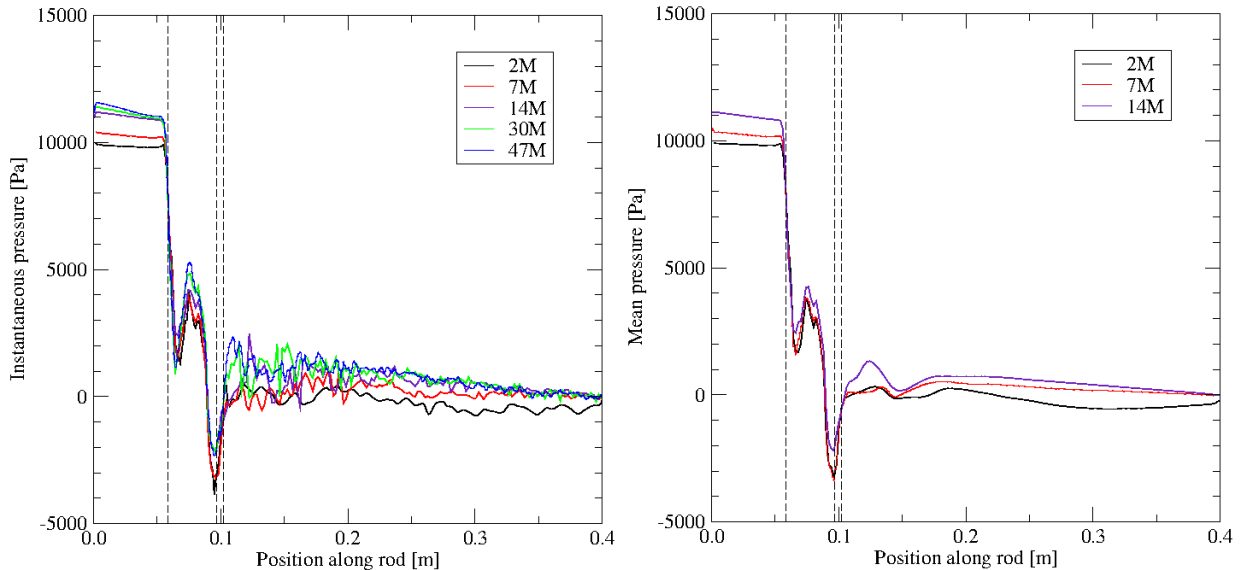


Figure 9: Instantaneous (left) and mean (right) pressure line plots for different meshes.

tion are quite different. The 2M mesh is too coarse to adequately capture the second pressure moment. At this point, we are not in a position to draw any conclusions regarding the grid-convergence of the RMS pressure. Regardless, the turbulent kinetic energy and the RMS pressure must decay downstream as no energy production occurs downstream of the mixing vanes.

The total force and its two components, the pressure and viscous forces, have been extracted in time on the central rod and the spacer. Surface forces are computed by integrating pressure and shear stress over the given surface:

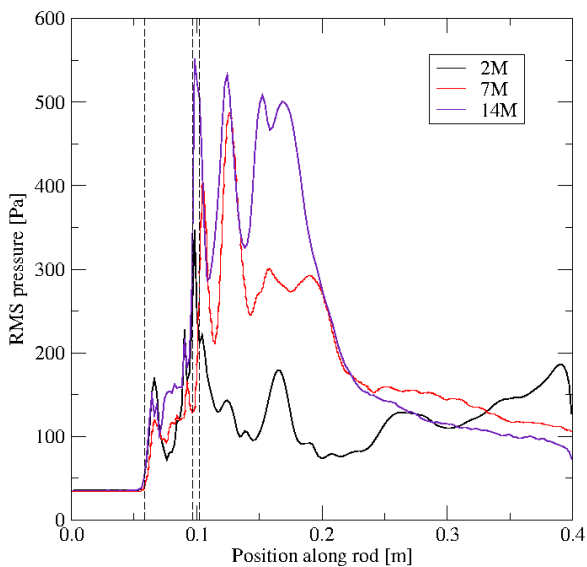
$$F_i(t) = - \int p(t) n_i dA + 2 \int \mu S_{ij}(t) n_j dA, \quad (4)$$

where \mathbf{F} , p , \mathbf{n} , A , and $S_{ij} = (v_{i,j} + v_{j,i})/2$ denote the total force, pressure, outward surface normal, surface area, and the strain rate of the instantaneous velocity, \mathbf{v} , respectively. This gives the force time history that can be used to compute power spectral distributions or fed directly into structural dynamics codes to compute the rod dynamics response and ultimately – wear. The total, pressure, and viscous force time-histories for the 7M case are presented in Figure 12, which shows that the mean forces are similar to those computed using the Cubit meshes presented in [19]. On the other hand the pressure

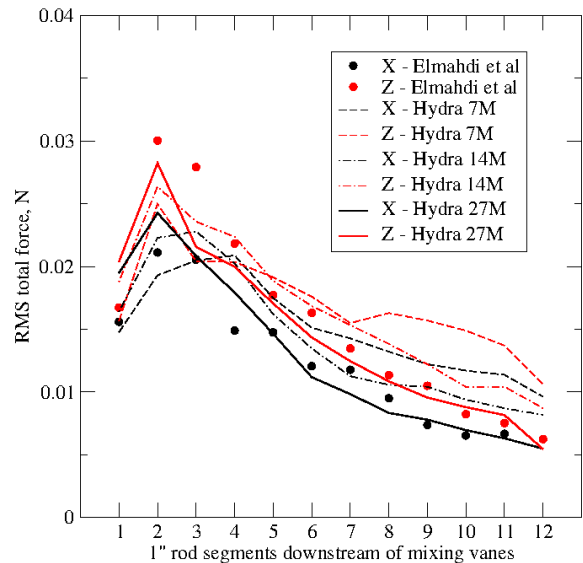
force acting on the central rod, probably the most important quantity for the GTRF problem, shows much larger fluctuations about the mean for the Spider mesh relative to the Cubit results.

The total forces have also been integrated in 12 one-inch segments downstream of the mixing vanes. This gives details on the spatial distribution of the forces loading the central rod and allows for a more direct comparison with the Star-CCM+ LES results in [20]. In Figure 10(b) the RMS total force is given in segments for the 7M, 14M, and 27M Spider meshes, compared to that of the Star-CCM+ LES results of Elmahdi, et al. [20] using a 47M-cell mesh. The 2M Spider mesh (not plotted) is inadequate to provide meaningful second moments of the force loading the rod. The RMS forces computed by Hydra-TH using the 7M, 14M, and 27M meshes are quite close to those for Star-CCM+, but obtained with significantly coarser meshes.

Additional insight into the fluctuating velocity field is found by examining the turbulent kinetic energy and Reynolds stresses, shown in Figure 11. In Figure 11(a), the downstream spatial evolution of the turbulent kinetic energy (TKE) is plotted for the 2M, 7M, and 14M meshes. Similar to the pressure fluctuations in Figure 10, the TKE, $k = \langle \mathbf{v} \cdot \mathbf{v} \rangle / 2$, peaks in the vicinity of the mixing vanes and stays at a relatively high value until ap-



(a) RMS pressure integrated over the full length of the central rod for three different meshes.



(b) RMS total force on the central rod integrated in 1-inch segments downstream of the mixing vanes. The Star-CCM+ results are from the LES calculations in [20].

Figure 10: Second moments of the pressure (integrated for the full length) and the total force (dominated by the pressure force) in segments.

proximately 0.2m downstream. This reinforces the earlier observation that the highest level of TKE occurs close to the downstream edge of mixing vanes. Figure 11(a) also indicates that the 2M-cell mesh is too coarse to produce a qualitatively correct TKE evolution; similar to the RMS pressure, the TKE should also decay downstream.

Figure 11(b) depicts the downstream evolution of the different components of the Reynolds stress tensor, $\langle \mathbf{v}\mathbf{v} \rangle$ for the 14M mesh. The figure shows that the flow downstream of the mixing vanes remains highly anisotropic until the end of the computational domain: almost all kinetic energy is in the streamwise component, $\langle vv \rangle$, of the velocity, $\mathbf{v} = (u, v, w)$, i.e., the streamwise fluctuations are large compared that of both cross-stream components, $\langle uu \rangle$, $\langle ww \rangle$, in x and z directions, respectively.

4.2. LES on the 5×5 Spider meshes

This section discusses the calculations for the 5×5 fuel-rod bundle. The geometry was provided in CAD format by Westinghouse, and corresponds to

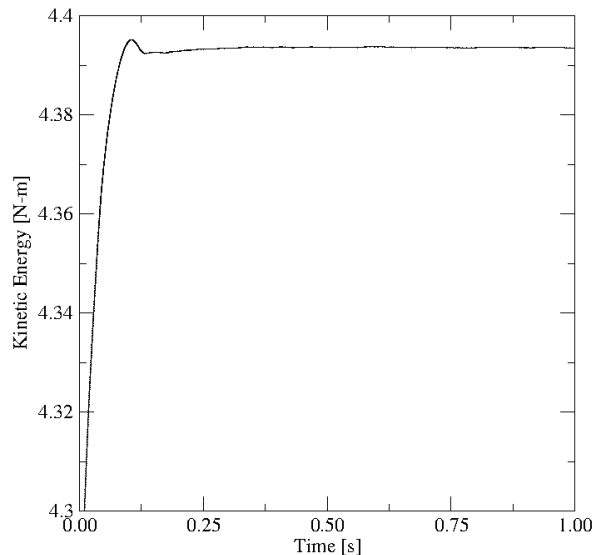
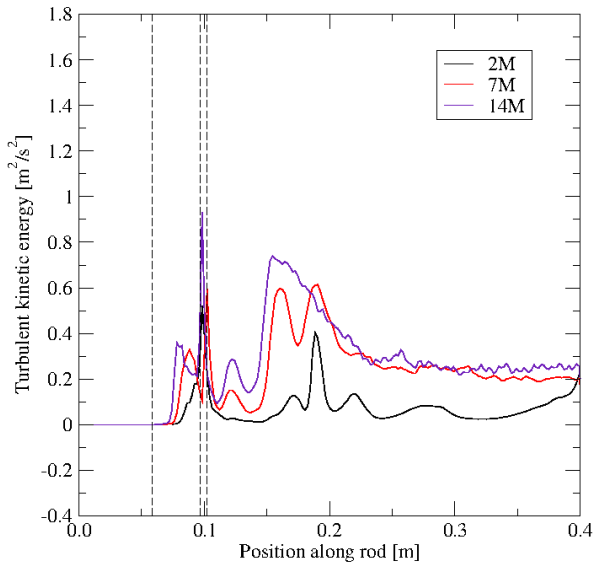
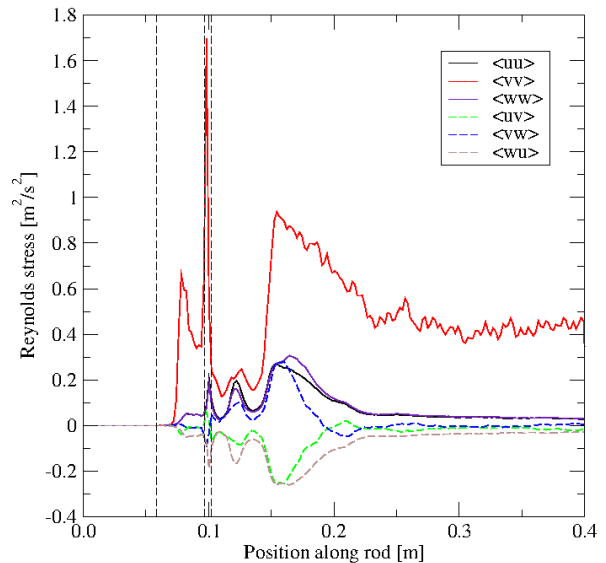


Figure 13: Domain-integrated kinetic energy, $\int \rho \mathbf{v} \cdot \mathbf{v} / 2 d\Omega$, vs. time for the 14M 5×5 rod bundle.



(a) Turbulent kinetic energy along the rod for three different meshes.



(b) Reynolds stress along the rod for the 14M mesh.

Figure 11: Second moments of the fluctuating velocity field for three different meshes.

the experimental configuration used at Texas A&M, where PIV measurements were carried out. The flow domain is shown in Figure 14. Not shown here are the exterior walls of the flow housing used in the experimental facility. Additional details on the experimental configuration and results may be found in Conner, et al. [23] and Yan, et al. [21].

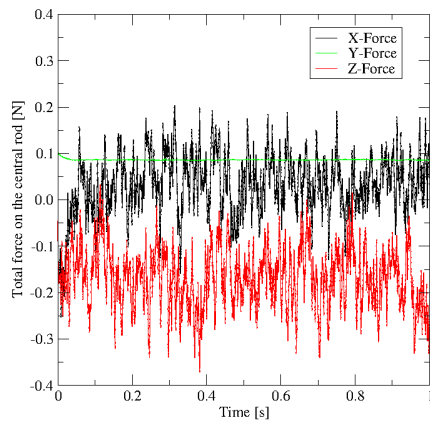
At the inlet of the flow domain, a constant prescribed velocity $(0.0, 2.48, 0.0)$ m/s is applied with the fluid properties for water at 24°C and atmospheric pressure. This corresponds to a Reynolds number of approximately 28,000 based on the hydraulic diameter for the rod bundle. At the surfaces of the flow housing, rods, support and spacer grids, no-slip/no-penetration velocity conditions were prescribed. Homogeneous Neumann conditions for velocity along with a zero-pressure condition were prescribed at the outflow plane. A fixed (maximum) $CFL = 4$ condition was used with automatic time-step control for all computations. The flow domain, meshed with Spider is illustrated in Figure 1(b).

Following the procedures to perform LES calculations on the 3×3 rod-bundle, outlined in [19], a series of preliminary coarse-mesh calculations were

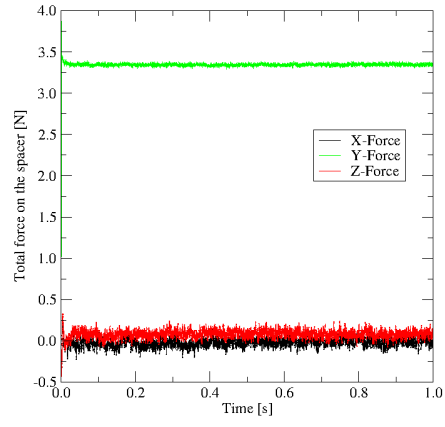
conducted to determine when a stationary turbulent state would be achieved and to test the sensitivity to mesh resolution and the time-step size. Figure 13 shows the domain-average kinetic energy, $\int \rho \mathbf{v} \cdot \mathbf{v} / 2 d\Omega$, as a function of time. Here Ω denotes the volume of the flow domain. Based on these preliminary calculations, we chose a time of approximately 0.2s as the starting point for collecting time-averaged flow statistics until the end of the simulation at $t = 1.0$ s. The initial 0.2s corresponds to approximately one flow transit after which the domain-integrated kinetic energy has reached a statistically stationary state.

In order to illustrate the impact of increasing mesh resolution on the flow, Figure 15 shows snapshots of the instantaneous helicity field for the 5×5 rod bundle. For the 14M mesh, there are relatively large coherent structures downstream of the support and spacer grid. In contrast, the flow structures captured by the 96M mesh are significantly smaller and appear more randomly distributed spatially. In both cases, the influence of the mixing vanes on the spacer grid is apparent.

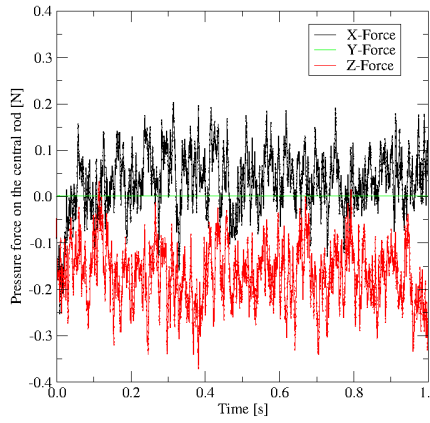
In order to compare to the experimental data, discussed in [21], a series of line plots were extracted



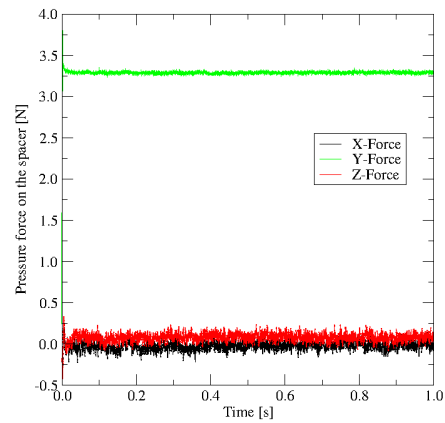
(a) Total force on the central rod.



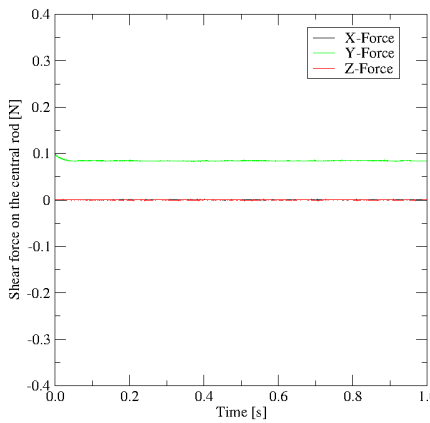
(b) Total force on the spacer.



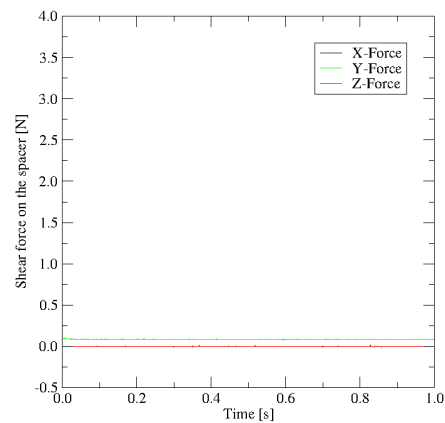
(c) Pressure force on the central rod.



(d) Pressure force on the spacer.



(e) Shear force on the central rod.



(f) Shear force on the spacer.

Figure 12: Total, pressure, and shear force time histories on the central rod and spacer for the 7M Spider mesh.

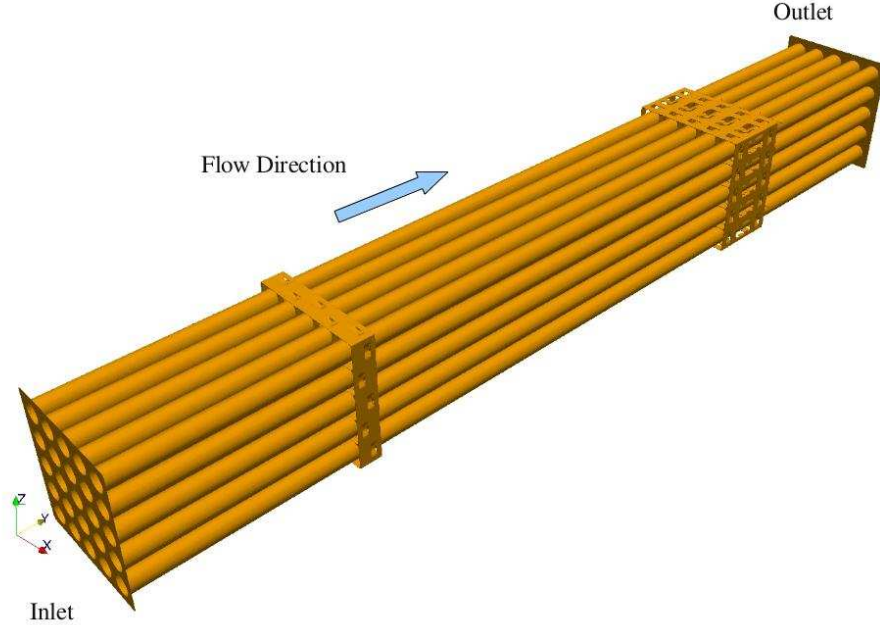


Figure 14: Flow domain for the 5×5 rod bundle showing the rods, the inlet/outlet planes, the support, and the spacer grid.

from the mean velocity field for the 14M-mesh 5×5 run at locations that fall in the planes of the PIV measurements. All line data were measured relative to the so-called “weld-nugget” located on the spacer grid. The “weld nugget” is located at 38.1 mm from the bottom of the spacer grid [24], as shown in Figure 16(a). The line-data extracted from the computation was located at the positions indicated in Figure 16. The coordinates of the sample points A – H are shown in Table 2 and are relative to the center of rod 13 in Figure 3 of [21]. In the flow direction, the line-data is extracted for $0.05 \leq y \leq 0.09$ m corresponding to the region where PIV data is available in the region downstream of the spacer grid.

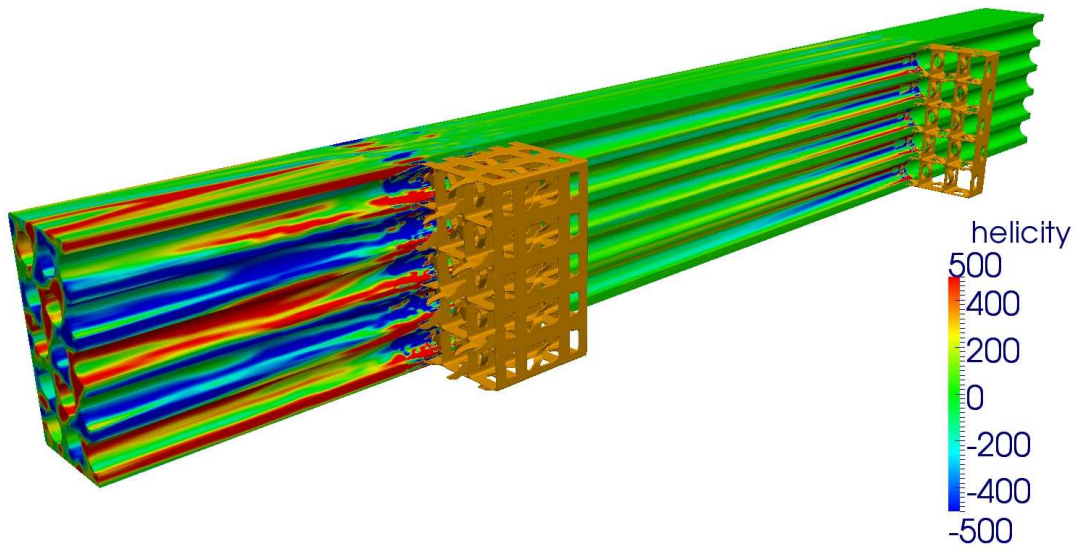
Following Yan, et al. [21], mean velocities are compared at points A, C, D, E, G, and H, as shown in Figure 17. Here, the streamwise velocity in the experiments corresponds to the y -velocity in the computation, while the lateral velocity corresponds to the x -velocity. Yan, et al. [21], estimated the systematic uncertainty in the velocities due to the PIV measurements, software acquisition, etc., to be a maximum of 0.199m/s. The statistical uncer-

Point	(x, z) Position [$10^{-3}m$]
A	(-6.3, 6.3)
B	(-6.3, 0.0)
C	(-6.3, -6.3)
D	(0.0, -6.3)
E	(6.3, -6.3)
F	(6.3, 0.0)
G	(6.3, 6.3)
H	(0.0, 6.3)

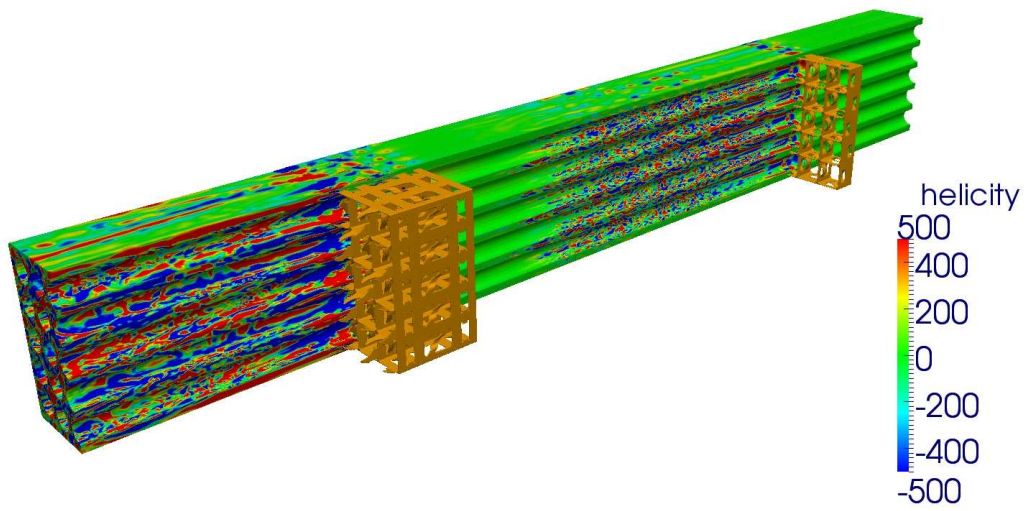
Table 2: Sample points A – H used to extract line-data for comparison with experimental data.

tainty, which is a function of the number of snapshots of the velocity, is estimated to be $\pm 0.167V_{\text{inlet}}$ in the lateral direction, and $\pm 0.15V_{\text{inlet}}$ in the axial direction, where $V_{\text{inlet}} = 2.48\text{m/s}$. All experimental data has been plotted with the uncertainty bounds provided by Dominguez-Ontiveros and Hassan, see also [23].

Line plots of the velocity are presented in Figure 17 for stations A – H. Inspection of Figure 17 indicates that experimental and computed x -velocities correlate relatively well, although for points A, C,



(a) 14M Mesh.



(b) 96M Mesh.

Figure 15: Snapshots of the instantaneous helicity field for the 14M and 96M element meshes.

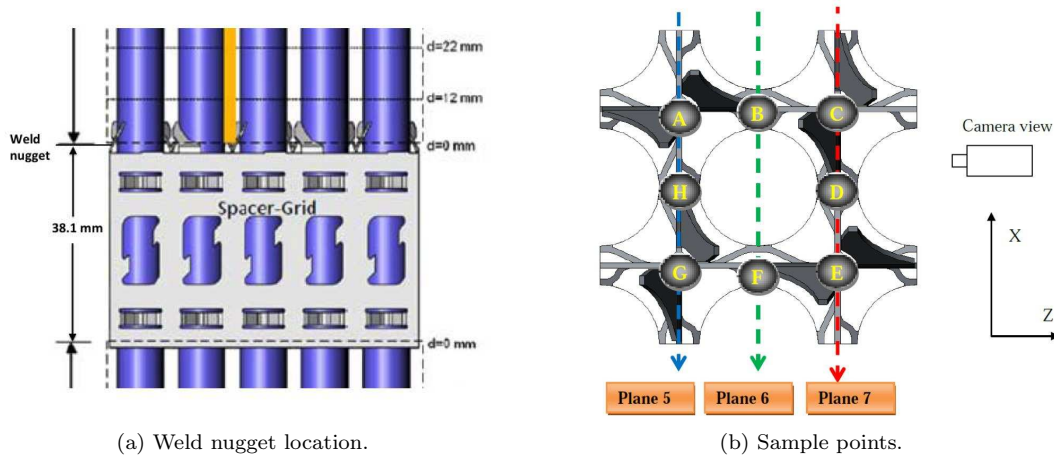


Figure 16: Locations relative to the “weld nugget” used for extracting data along planes 5, 6 and 7. (Reproduced from [21]) without permission.)

E, and G, the x -velocities are near zero. For this relatively coarse mesh, the streamwise velocities do not compare as well, however, the general trends appear to be similar. Note that typically, the y -velocity is overpredicted in the streamwise directions, which is not surprising for this coarse mesh. In comparison, the mesh used by Yan, et al. [21], contained approximately 76M hexahedral elements.

The line plots of velocity for the 96M mesh are presented in Figure 18 for stations A – H. In comparison to the velocity profiles in Figure 17, the 96M results match the experimental data more closely at all points A – H. However, the stream-wise velocity still appears to be slightly overpredicted. In contrast, the x -velocities fall within the uncertainty bounds for points A, C, E, and G, while the x -velocities at points D and H have similar profiles, but are not quite within the uncertainty bounds. Overall, the 96M results compare very well to the experimental data.

Time-averaged velocities in plane-5, see Figure 16 from [23], are shown in Figure 19 with the computed time-averaged mean velocity fields. Similarly, the experimental and computed mean velocity fields on plane-7 are shown in Figure 20. The data in the figures have been scaled relative to the 2.48m/s inlet velocity. The peak velocities in the axial direction are slightly under-predicted in the Hydra-TH computations, while the lateral velocities are slightly over-predicted. This is likely due to the very coarse mesh used in this LES calculation. While the peak velocities appear to be relatively close to those found experimentally, inspection of Figures 19 and

20 indicates that the deflection in the velocity vectors due to the mixing vanes and the flow housing is well-captured by the simulation.

5. Summary

A series of isothermal turbulent flow calculations have been carried out using Hydra-TH, a thermal hydraulics code developed at Los Alamos National Laboratory. Our main goal is to understand the fluid dynamics of the flow-induced vibration problem leading to grid-to-rod-fretting (GTRF), a major cause of nuclear plant shutdowns.

We found that the mesh quality is extremely important for the accurate computation of turbulent fluctuations and the resulting dynamic load on the fuel rods.

Progress is reported here on several fronts towards a simulation capability for advanced thermal-hydraulics methods in the nuclear engineering industry:

1. *Mesh generation.* Numeca’s Hexpress/Hybrid mesh generator, a.k.a. “Spider”, has been used for the first time to generate computational meshes for the GTRF problem. Spider is easy to use, fast, and automatically generates high-quality meshes with optional power-law-graded boundary layers. Output is saved in the latest HDF5/ExodusII format, capable of storing meshes in the billion-cell range. Spider can also generate meshes, in one run, for both fluid and

solid parts of a domain, which allows mesh generation for fluid-structure interaction and conjugate heat transfer problems [25].

2. *Quantitative a priori mesh assessment.* A method for quantitative assessment of complex unstructured meshes with no-slip walls has been developed and used to assess a series of meshes generated for the GTRF problem by two mesh generators.
3. *New GTRF flow calculations.* A series of turbulent flow simulations have been carried out on both 3×3 and 5×5 rod bundle geometries. Various statistics of the fluctuating flow field have been analyzed and compared to data from computations carried out by Westinghouse using Star-CCM+ and from experiments at Texas A&M University.
4. *RMS forces on rod order-of-magnitude different between Cubit and Spider meshes.* Arguably the most important quantity for coupling the current results to a structural code is the fluctuations of the pressure force loading the rods. Using the same algorithm and code, we found the predicted RMS forces, integrated for the whole rod, an order of magnitude larger using the higher-quality Spider meshes compared to the Cubit meshes, see [19].

6. Future work

Future work on GTRF will focus on coupling the structural response of the fuel rods at different dynamic levels of approximation (e.g. one-way, two-way), along with coupling different wear models developed by collaborators in the CASL project. The largest mesh we have run to date for the 3×3 and 5×5 problems have approximately 47 and 96 million computational cells, respectively. In order to adequately resolve the turbulent flow features and the heat transfer along the turbulent boundary layers, we believe meshes of 100 million to 1 billion elements may be required, depending on plant operating conditions. To incorporate the effects of boiling, multiphase flow models are also being developed and implemented in the Hydra software toolkit.

7. Acknowledgments

This research is supported by the Consortium for Advanced Simulation of Light Water Reactors (CASL), a U.S. Department of Energy Innovation

Hub. The authors gratefully acknowledge the help in visualization and high-performance computing issues from Ross Toedte and Ramanan Sankaran, respectively, at Oak Ridge National Laboratory; Elvis Dominguez-Ontiveros and Yassin Hassan at Texas A&M University for providing the experimental data; and the help in meshing from Roger Pawlowski and Tom Smith at Sandia National Laboratories.

References

References

- [1] M. P. Païdousis, A review of flow-induced vibrations in reactors and reactor components, *Nuclear Engineering and Design* 74 (1982) 31–60.
- [2] M. J. Pettigrew, L. N. Carlucci, C. E. Taylor, N. J. Fisher, Flow-induced vibration and related technologies in nuclear technologies, *Nuclear Engineering and Design* 131 (1991) 81–100.
- [3] T. Ikeno, T. Kajishima, Decay of swirling turbulent flow in rod-bundle, *Journal of Fluid Science and Technology* 1 (2006) 36–47.
- [4] S. Benhamadouche, P. Moussou, C. L. Maitre, CFD estimation of the flow-induced vibrations of a fuel rod downstream of a mixing grid, in: *PVP 2009 ASME Pressure Vessels and Piping 2009/Creep 8 Conference*, Prague, Czech Republic, 2009.
- [5] K.-T. Kim, The study on grid-to-rod fretting wear models for PWR fuel, *Nuclear Engineering and Design* 239 (2009) 2820–2824.
- [6] K.-T. Kim, A study on the grid-to-rod fretting wear-induced fuel failure observed in the 16×16 KOFA fuel, *Nuclear Engineering and Design* 240 (2010) 756–762.
- [7] K.-T. Kim, The effect of fuel rod supporting conditions on fuel rod vibration characteristics and grid-to-rod fretting wear, *Nuclear Engineering and Design* 240 (2010) 1886–1391.
- [8] M. E. Conner, E. Baglietto, A. M. Elmahdi, Cfd methodology and validation for single-phase flow in pwr fuel assemblies, *Nuclear Engineering and Design* 240 (2010) 2088–2095.
- [9] J. Yan, K. Yuan, E. Tatli, Z. Karoutas, A new method to predict grid-to-rod fretting in a PWR fuel assembly inlet region, *Nuclear Engineering and Design* 241 (2011) 2974–2982.
- [10] X. Zhang, S. D. Yu, Large eddy simulation of turbulent flow surrounding two simulated CANDU fuel bundles, *Nuclear Engineering and Design* 241 (2011) 3553–3572.
- [11] A. Bhattachary, S. D. Yu, G. Kwall, Numerical simulation of turbulent flow through a 37 element CANDU fuel bundle, *Annals of Nuclear Energy* 40 (2012) 87–105.
- [12] S. Delafontaine, G. Ricciardi, Fluctuating pressure calculation induced by axial flow through mixing grid, *Nuclear Engineering and Design* 242 (2012) 233–246.
- [13] Z. G. Lui, Y. Liu, J. Lu, Numerical simulation of the fluid-structure interaction for two simple fuel assemblies, *Nuclear Engineering and Design* 258 (2013) 1–12.
- [14] A. Mohany, M. Hassan, Modeling of fuel bundle vibration and the associated fretting wear in a CANDU

- fuel channel, Nuclear Engineering and Design *in press*Article in press.
- [15] S. B. Pope, Turbulent flows, Cambridge University Press, Cambridge, 2000.
 - [16] P. M. Gresho, On the theory of semi-implicit projection methods for viscous incompressible flow and its implementation via a finite element method that also introduces a nearly consistent mass matrix. part 1: Theory, International Journal for Numerical Methods in Fluids 11 (1990) 587–620.
 - [17] P. M. Gresho, S. T. Chan, On the theory of semi-implicit projection methods for viscous incompressible flow and its implementation via a finite element method that also introduces a nearly consistent mass matrix. part 2: Implementation, International Journal for Numerical Methods in Fluids 11 (1990) 621–659.
 - [18] M. A. Christon, Hydra-TH Theory Manual, Tech. Rep. LA-UR 11-05387, Los Alamos National Laboratory (September 2011).
 - [19] M. A. Christon, J. Bakosi, N. Barnett, M. M. Francois, R. B. Lowrie, Initial Assessment of Hydra-TH on Grid-to-Rod Fretting Problems (thm.cfd.p4.01), Tech. Rep. LA-UR-11-07034, Los Alamos National Laboratory (2011).
 - [20] A. M. Elmahdi, R. Lu, M. E. Conner, Z. Karoutas, E. Baglietto, Flow induced vibration forces on a fuel rod by les cfd analysis, in: The 14th International Topical Meeting on Nuclear Reactor Thermal Hydraulics (NURETH-14), Hilton Toronto Hotel, Toronto, Ontario, Canada, 2011.
 - [21] J. Yan, M. E. Conner, R. A. Brewster, Z. E. Karoutas, E. E. Dominguez-Ontiveros, Y. A. Hassan, Validation of CFD method in predicting steady and transient flow field generated by PWR mixing vane grid, in: CFD4NRS-4 – The Experimental Validation and Application of CFD and CMFD Codes in Nuclear Reactor Technology, OECD/NEA & International Atomic Energy Agency (IAEA) Workshop, Daejeon, Korea, 2012.
 - [22] F. Nicoud, F. Ducros, [Subgrid-scale stress modelling based on the square of the velocity gradient tensor](#), Flow, Turbulence and Combustion 62 (1999) 183–200, 10.1023/A:1009995426001.
URL <http://dx.doi.org/10.1023/A:1009995426001>
 - [23] M. E. Conner, E. E. Dominguea-Otiveros, Y. A. Hassan, Hydraulic benchmark data for pwr mixing vane grid, in: The 14th International Topical Meeting on Nuclear Reactor Thermal Hydraulics, Toronto, Canada, 2011.
 - [24] J. Yan, personal communication (August 2012).
 - [25] Numeca Inc., personal communication (July 2012).

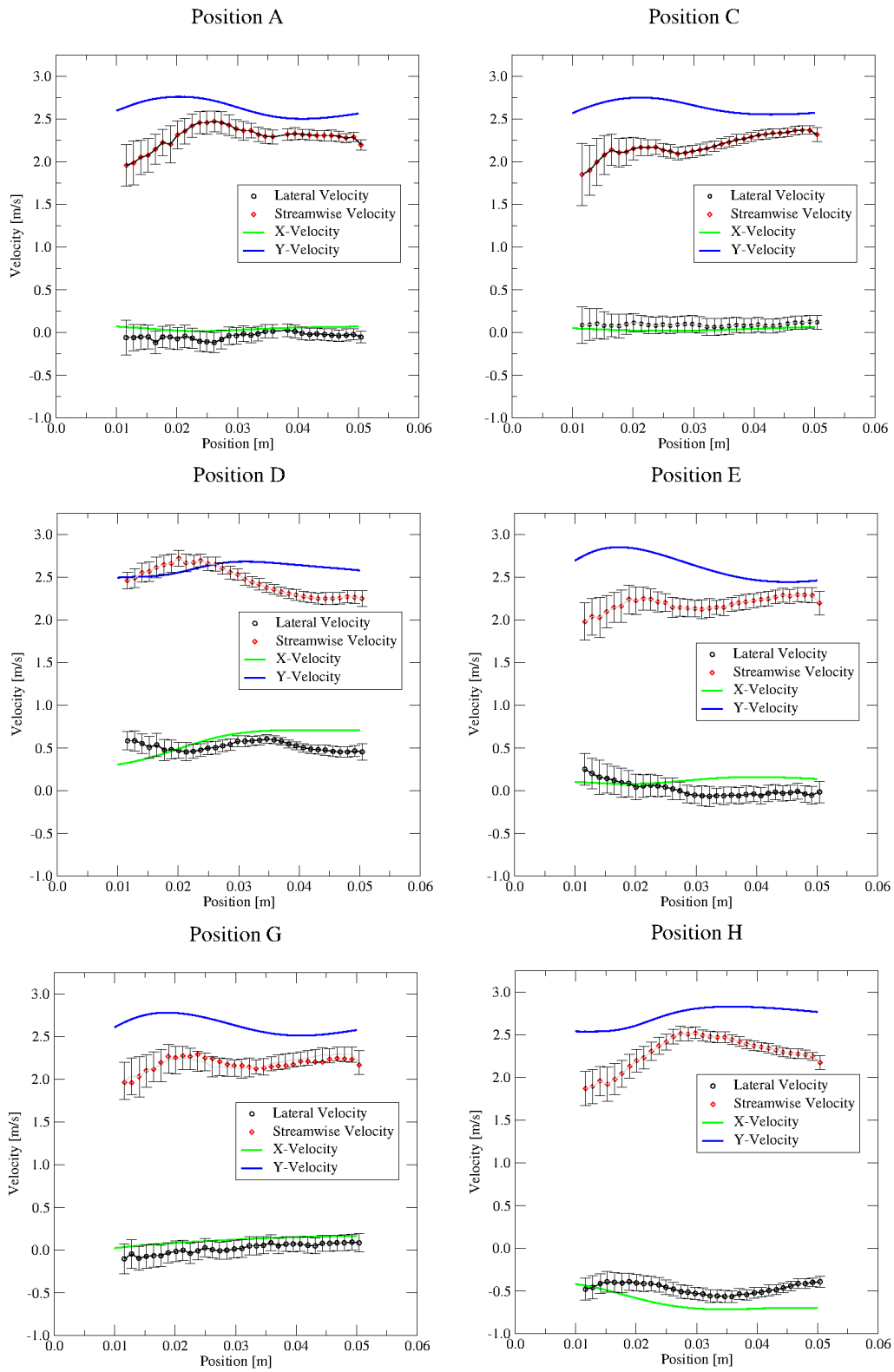


Figure 17: Mean axial and lateral velocity profiles at positions A, C, D, E, G and H for the 14M mesh.

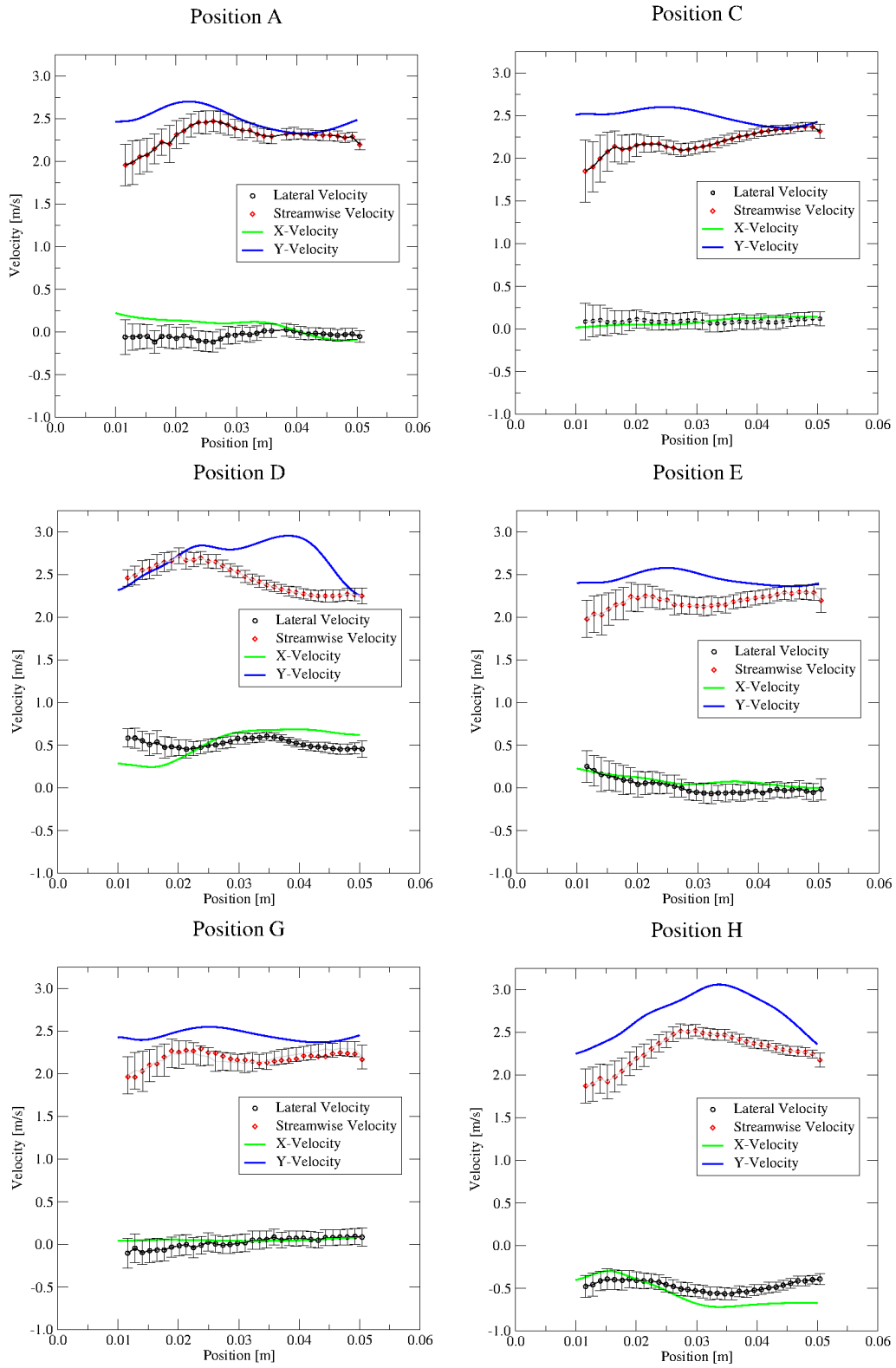


Figure 18: Mean axial and lateral velocity profiles at positions A, C, D, E, G and H for the 96M mesh.

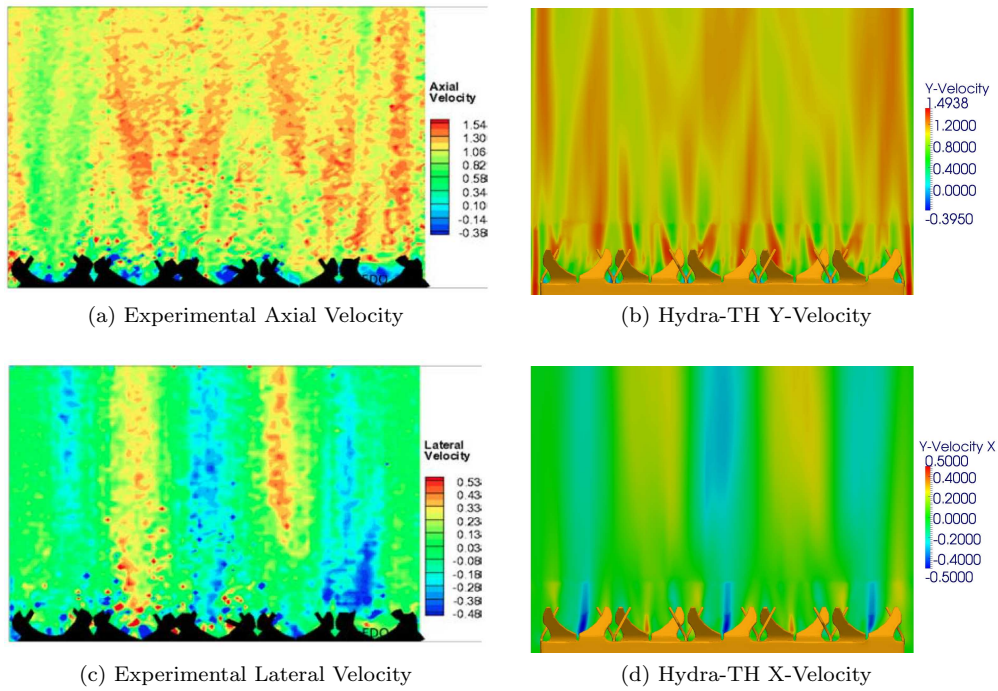


Figure 19: Experimental and computed axial (y-direction) time-averaged velocities on plane 5. Velocity magnitude has been scaled relative to the 2.48 m/s inlet velocity.

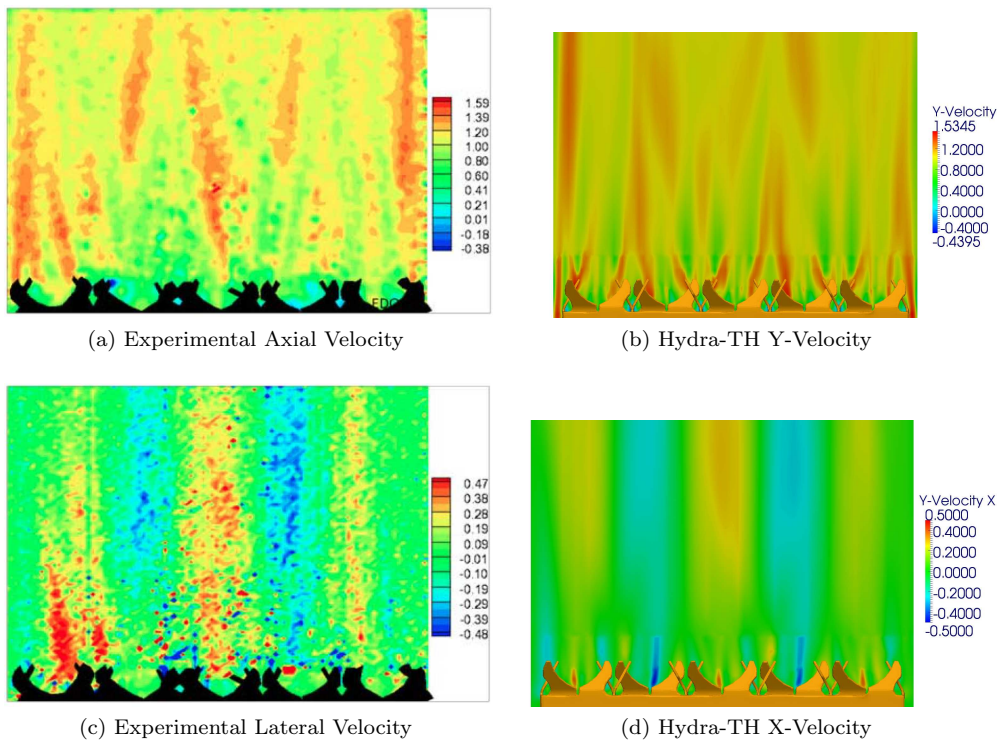


Figure 20: Experimental and computed axial (y-direction) time-averaged velocities on plane 7. Velocity magnitude has been scaled relative to the 2.48 m/s inlet velocity.